

Pupil Mapping in 2-D for High-Contrast Imaging

Robert J. Vanderbei

Operations Research and Financial Engineering, Princeton University

rvdb@princeton.edu

and

Wesley A. Traub

Harvard-Smithsonian Center for Astrophysics

wtraub@cfa.harvard.edu

ABSTRACT

Pupil-mapping is a technique whereby a uniformly-illuminated input pupil, such as from starlight, can be mapped into a non-uniformly illuminated exit pupil, such that the image formed from this pupil will have suppressed sidelobes, many orders of magnitude weaker than classical Airy ring intensities. Pupil mapping is therefore a candidate technique for coronagraphic imaging of extrasolar planets around nearby stars. The pupil mapping technique is lossless, and preserves the full angular resolution of the collecting telescope, so it could possibly give the highest signal-to-noise ratio of any proposed single-telescope system for detecting extrasolar planets. A planet fainter than 10^{-10} times its parent star, and as close as about $2\lambda/D$ should be detectable. We derive the 2-dimensional equations of pupil mapping for both 2-mirror and 2-lens systems. We give examples for both cases. We derive analytical estimates of aberration in a 2-mirror system, and show that the aberrations are essentially corrected with an added reversed set of mirrors.

Subject headings: Extrasolar planets, coronagraphy, point spread function, pupil mapping, apodization

1. Introduction

To successfully detect and characterize extrasolar terrestrial planets around nearby stars, it is necessary to isolate the light of a planet from that of the parent star to better than about 10^{-10}

at visible wavelengths or 10^{-6} at thermal infrared wavelengths (DesMarais et al. (2002)). Two general types of space-based instruments have been proposed to do this, visible coronagraphs and infrared interferometers.

At present, NASA plans to launch the Terrestrial Planet Finder-Coronagraph (TPF-C) in 2014, and the Terrestrial Planet Finder-Interferometer (TPF-I) in 2019. ESA plans to launch an infrared interferometer, DARWIN, around 2015. Each of these observatories appears to be feasible using current or expected technology, and for each there are several alternative architectures now under study. The present paper discusses the underlying mathematical principle of the coronagraph concept known as *pupil mapping* (Traub and Vanderbei (2003)), alternatively called *intrinsic apodization* (Goncharov et al. (2002)) or *phase-induced amplitude apodization (PIAA)* (Guyon (2003), Galicher et al. (2004)).

The basic idea of pupil mapping is that the uniform intensity of starlight falling on the input pupil of a telescope can be mapped, ray by ray, to a non-uniform intensity in an exit pupil, such that the image of a star will be highly concentrated with minimal sidelobes. The goal is to reduce the sidelobes to less than 10^{-10} within a very few diffraction widths from the central star. This permits us to separate starlight from planet-light. For perspective, sidelobes less than 10^{-10} are roughly 8 orders of magnitude lower than the Airy-ring pattern that would be expected from an idealized conventional telescope image.

Several other coronagraphic methods have been suggested. One of the first was the idea of a square apodized pupil (Nisenson and Papaliolios (2001)), in which the transmission function of the pupil is tapered to zero at the edges, thereby reducing the sidelobes, but at a loss of light and angular resolution. Another idea is the shaped pupil (Spergel (2000), Vanderbei et al. (2003a,b,c, 2004)), in which the pupil is covered by an opaque mask that has carefully-shaped transmitting cut-outs, thereby strongly reducing the sidelobes in two azimuthally-opposite segments, but again at a loss of light as well as some loss of angular resolution. A different approach was taken by Kuchner and Traub (2002), Kuchner and Spergel (2003), and Kuchner et al. (2004), who proposed a family of image-plane band-limited masks that would block starlight and transmit planet light, with little loss of planet light and nearly full angular resolution. Yet another idea was suggested by Levine et al. (2003) who combine pupil-shearing with single-mode fibers, a combination that also potentially has good transmission and angular resolution. Other methods have also been proposed, some of which are more limited in spectral range; see, for example, Aime and Soummer (2003).

Even before Guyon first suggested pupil mapping for TPF-C, there was an abundant literature on the topic of beam-shaping, in both the radio astronomy community (in order to optimally couple a telescope beam into a detector horn), and in the laser community (to reshape the Gaussian beam from a laser into a more generally useful uniform-intensity beam). The laser beam shaping is closely related to the present pupil mapping for astronomy, because the laser beam work par-

ticularly aimed at maintaining a flat wavefront after the shaping optics. In particular we mention the U.S. patent awarded to Kreuzer (1969), and a more recent, but representative, application of this work by Hoffnagle and Jefferson (2003). In fact, one of the equations that we derive in the present paper (equations (53) and (54) in Theorem 2), for the case of pupil mapping with lenses, is identical to that derived by Kreuzer, the only difference being that the latter was trying to make a uniform-intensity beam from a Gaussian one, and we are trying to do essentially the reverse of that.

The present paper is an extension of our previous one (Traub and Vanderbei (2003)), in that we move from an idealized 1-D treatment to the more physical 2-D case, in addition to which we now also present equations for pupil mapping with lenses as well as mirrors. We furthermore include an analytical development of off-axis aberrations, and a method for removing the aberrations of off-axis images. We give several illustrative examples of pupil mapping, including a section showing how one simple type of pupil-mapping can directly yield the entire family of Cassegrain and Gregorian paraboloid-based telescopes, including the simple plane-mirror periscope as a special case.

Our approach in this paper is the same as in Traub and Vanderbei (2003), namely to develop the analytical basis of pupil mapping, and explore the consequences. For some questions, including that of fabrication, it will be necessary to carry out numerical investigations, which we defer to a future paper.

The organization of the present paper is as follows. In Section 2, we define the ray-by-ray mapping function R . In Section 3, we derive the differential equations describing the mirror surfaces in terms of R . In Section 4, we show how R can be calculated from the function A^2 , where A^2 is the point-by-point ratio of output to input intensity across the pupil. In Section 5, we give three examples of pupil-mapping, for constant, Gaussian, and prolate-spheroidal-like functions. In Section 6, we extend the theory to include on-axis mirror systems. In Section 7, we extend the theory to 2-lens systems. In Section 8, we show how to modify the equations to apply to elliptically shaped pupils. In Section 9, we estimate the magnitude of off-axis aberrations in 2-mirror systems and show that the aberrations are nearly eliminated with a pair of identical but reversed mirrors.

2. Pupil Mapping

Consider a 2-mirror optical pupil-mapping system endowed with a Cartesian coordinate system in which the z -axis corresponds to the optical axis so that the pupil and image planes are parallel to the (x, y) -plane. The first mirror's projection onto the (x, y) -plane is a circle of radius a

centered at $(0, 0)$:

$$\mathcal{M}_1 = \{(x, y) : x^2 + y^2 \leq a^2\}. \quad (1)$$

The second mirror has radius \tilde{a} and is shifted along the x -axis by a distance δ . Its projection on the (\tilde{x}, \tilde{y}) -plane is

$$\mathcal{M}_2 = \{(\tilde{x}, \tilde{y}) : (\tilde{x} - \delta)^2 + \tilde{y}^2 \leq \tilde{a}^2\}. \quad (2)$$

The displacement δ can be any real value, but if the mirrors are nonoverlapping then we need

$$|\delta| \geq a + \tilde{a}. \quad (3)$$

If $\delta = 0$, then the optics are concentric. We show two such examples; for mirrors in Section 6.2, and for lenses in Section 7. We introduce polar coordinates r and θ for \mathcal{M}_1 , and \tilde{r} and θ for \mathcal{M}_2 . Hence,

$$x = r \cos \theta, \quad y = r \sin \theta \quad (4)$$

$$\tilde{x} = \tilde{r} \cos \theta + \delta, \quad \tilde{y} = \tilde{r} \sin \theta. \quad (5)$$

Note that $r = 0$ and $\tilde{r} = 0$ refer to physically different locations (the centers of \mathcal{M}_1 and \mathcal{M}_2 , respectively), but $x = 0$ and $\tilde{x} = 0$ are the same physical location. The mirror surfaces are at $z = h(x, y)$ for the first mirror and $\tilde{z} = \tilde{h}(\tilde{x}, \tilde{y})$ for the second mirror. Light enters the system from above, reflects upward off from the first mirror and then impinges on the second mirror, which reflects it back downward.

A pupil mapping is determined by specifying a one-to-one and onto mapping between the two mirrors, or equivalently between their two projections \mathcal{M}_1 and \mathcal{M}_2 . In general, such mappings could be rather elaborate. To keep the design (and analysis) simple, we assume that polar angle θ on the first mirror maps to the same polar angle on the second one. Hence, the pupil mapping is completely determined by giving a function \tilde{R} from mirror-one radii to mirror-two radii. Hence, we have

$$\tilde{r} = \tilde{R}(r). \quad (6)$$

To be one-to-one, \tilde{R} must map $[0, a]$ monotonically onto $[0, \tilde{a}]$. In such a case, there is an inverse function R :

$$r = R(\tilde{r}). \quad (7)$$

The fact that these functions are inverse to each other is expressed as

$$\tilde{R}(R(\tilde{r})) = \tilde{r}, \quad R(\tilde{R}(r)) = r. \quad (8)$$

3. Mirror Shapes

Let \vec{I} and \vec{R} denote the unit incidence and unit reflection vectors at a mirror surface. Let \vec{N} denote a vector normal to a point on a mirror surface. At point $(x, y, h(x, y))$ on the first mirror, these vectors are

$$\vec{I} = \begin{bmatrix} 0 \\ 0 \\ 1 \end{bmatrix}, \quad \vec{N} = \begin{bmatrix} -h_x \\ -h_y \\ 1 \end{bmatrix}, \quad \vec{R} = \begin{bmatrix} \tilde{x} - x \\ \tilde{y} - y \\ \tilde{h} - h \end{bmatrix} \frac{1}{S(x, y, \tilde{x}, \tilde{y})}, \quad (9)$$

where $h = h(x, y)$, $\tilde{h} = \tilde{h}(\tilde{x}, \tilde{y})$, subscripts x and y denote partial differentiation with respect to the indicated variable, i.e.

$$h_x(x, y) = \frac{\partial h(x, y)}{\partial x}, \quad (10)$$

and

$$S(x, y, \tilde{x}, \tilde{y}) = \sqrt{(\tilde{x} - x)^2 + (\tilde{y} - y)^2 + (\tilde{h} - h)^2} \quad (11)$$

denotes the distance from point (x, y, h) on the first mirror to the corresponding point $(\tilde{x}, \tilde{y}, \tilde{h})$ on the second mirror. The shape of the first mirror is determined by requiring that \vec{I} , \vec{N} , and \vec{R} are coplanar and that angle of incidence equals angle of reflection. In other words, it is required that $\vec{I} \times \vec{N} = -\vec{R} \times \vec{N}$. Computing these cross products, we get

$$\vec{I} \times \vec{N} = \begin{bmatrix} h_y \\ -h_x \\ 0 \end{bmatrix} \quad \vec{R} \times \vec{N} = \begin{bmatrix} \tilde{y} - y + h_y(\tilde{h} - h) \\ x - \tilde{x} - h_x(\tilde{h} - h) \\ h_x(\tilde{y} - y) - h_y(\tilde{x} - x) \end{bmatrix} \frac{1}{S}, \quad (12)$$

where S is shorthand for $S(x, y, \tilde{x}, \tilde{y})$. Equating the first two components, we can easily solve for h_x and h_y :

$$h_x = \frac{x - \tilde{x}}{S + \tilde{h} - h}, \quad h_y = \frac{y - \tilde{y}}{S + \tilde{h} - h}. \quad (13)$$

Because the light after reflecting off from the second mirror should be traveling in the z direction once again, it follows from simple geometry that

$$\tilde{h}_{\tilde{x}} = h_x \quad \text{and} \quad \tilde{h}_{\tilde{y}} = h_y. \quad (14)$$

As in our earlier paper Traub and Vanderbei (2003), we have the following important lemma that tells us that the optical path length for an on-axis source through the system is constant.

Lemma 1 $P_0 = S + \tilde{h} - h$ is a constant.

Proof. The quantity of interest, $S + \tilde{h} - h$, is a shorthand for $S(x, y, \tilde{x}, \tilde{y}) + \tilde{h}(\tilde{x}, \tilde{y}) - h(x, y)$. Although it appears that there are four independent variables, there are in fact only two since variables x and y can be considered to be functions of \tilde{x} and \tilde{y} (or vice versa). Hence, we need only show that the derivatives with respect to \tilde{x} and \tilde{y} vanish. Using (14), it is easy to check that

$$\frac{d}{d\tilde{x}} \left(S(x, y, \tilde{x}, \tilde{y}) + \tilde{h}(\tilde{x}, \tilde{y}) - h(x, y) \right) = G(\tilde{x}, \tilde{y}) \left(1 - \frac{\partial x}{\partial \tilde{x}} \right) - K(\tilde{x}, \tilde{y}) \frac{\partial y}{\partial \tilde{x}}, \quad (15)$$

where

$$G(\tilde{x}, \tilde{y}) = \frac{\tilde{x} - x + h_x(\tilde{h} - h)}{S} + h_x \quad (16)$$

and

$$K(\tilde{x}, \tilde{y}) = \frac{\tilde{y} - y + h_y(\tilde{h} - h)}{S} + h_y. \quad (17)$$

Putting the two right-hand terms over a common denominator (S) and then substituting the expressions in (13) for h_x and h_y , it is easy to see that both G and K vanish. Hence, the derivative with respect to \tilde{x} vanishes. That the derivative with respect to \tilde{y} also vanishes is shown in precisely the same way. \square

An important consequence of this Lemma is a simple decoupling of the differential equations for the mirror shapes.

Theorem 1 *The shape of the first mirror is determined by the following pair of ordinary differential equations:*

$$h_x = \frac{x - \tilde{x}}{P_0}, \quad h_y = \frac{y - \tilde{y}}{P_0}, \quad (18)$$

where \tilde{x} and \tilde{y} are known functions of x and y . Similarly, the shape of the second mirror is determined by:

$$\tilde{h}_{\tilde{x}} = \frac{x - \tilde{x}}{P_0}, \quad \tilde{h}_{\tilde{y}} = \frac{y - \tilde{y}}{P_0}, \quad (19)$$

where x and y are known functions of \tilde{x} and \tilde{y} .

Proof. The equations are an immediate consequence of Lemma 1, (13), and (14). The “known” formulae relating \tilde{x} and \tilde{y} to x and y are easy to compute from the functions R and \tilde{R} . For example,

$$\tilde{x} = \tilde{r} \cos \theta + \delta = \frac{\tilde{r}}{r} r \cos \theta + \delta = \frac{\tilde{R}(r)}{r} x + \delta = \frac{\tilde{R}(\sqrt{x^2 + y^2})}{\sqrt{x^2 + y^2}} x + \delta. \quad (20)$$

The other relations are derived in a similar manner. \square

We have two approaches that can be followed in solving for the mirror shapes. First, we can solve each of equations (18) and (19) separately; an advantage of this, for the case when the differential equations must be solved numerically, is that we can choose the x or \tilde{x} coordinates independently, say with equal step sizes. Second, we can solve either (18) or (19), analytically or numerically, then find the other shape algebraically, as follows. From Lemma 1 we can solve for S and then square it to see that

$$S^2 = \left(P_0 - \tilde{h} + h\right)^2 = P_0^2 - 2P_0(\tilde{h} - h) + (\tilde{h} - h)^2. \quad (21)$$

Substituting $S^2 = (\tilde{x} - x)^2 + (\tilde{y} - y)^2 + (\tilde{h} - h)^2$, we see that the quadratic terms involving $\tilde{h} - h$ cancel and so we are left with a simple calculation for the difference:

$$\tilde{h} - h = \frac{P_0}{2} - \frac{(\tilde{x} - x)^2 + (\tilde{y} - y)^2}{2P_0}. \quad (22)$$

Hence, if we already know either \tilde{h} or h , we can use (22) to compute the other one. An advantage of this method, for the case of numerical solutions of the differential equations, is that the step size chosen for one mirror will automatically map to the corresponding step on the other mirror. Another way to say this is that the ray intersections on the first mirror map to the intersections of the same rays on the second mirror, facilitating visualization of the ray paths.

Let us return now to polar coordinates. Put

$$\tilde{H}(\tilde{r}, \theta) = \tilde{h}(\tilde{x}, \tilde{y}), \quad (23)$$

where $\tilde{x} = \tilde{r} \cos \theta + \delta$ and $\tilde{y} = \tilde{r} \sin \theta$. Using (4) and (5), we get the following differential equations for \tilde{H} :

$$\tilde{H}_{\tilde{r}} = \tilde{h}_{\tilde{x}} \cos \theta + \tilde{h}_{\tilde{y}} \sin \theta = \frac{(x - \tilde{x}) \cos \theta + (y - \tilde{y}) \sin \theta}{P_0} = \frac{(r - \tilde{r}) - \delta \cos \theta}{P_0} \quad (24)$$

and

$$\tilde{H}_{\theta} = -\tilde{h}_{\tilde{x}} \tilde{r} \sin \theta + \tilde{h}_{\tilde{y}} \tilde{r} \cos \theta = \frac{-(x - \tilde{x}) \tilde{r} \sin \theta + (y - \tilde{y}) \tilde{r} \cos \theta}{P_0} = \frac{\delta \tilde{r} \sin \theta}{P_0} = \frac{\delta \tilde{y}}{P_0}. \quad (25)$$

We can integrate in the radial direction along \tilde{r} (holding θ constant) to get

$$\tilde{H}(\tilde{r}, \theta) = \tilde{H}(0, 0) + \int_0^{\tilde{r}} \frac{R(u) - u - \delta \cos \theta}{P_0} du = \tilde{H}(0, 0) + \frac{1}{P_0} \int_0^{\tilde{r}} (R(u) - u) du - \frac{\delta \tilde{r} \cos \theta}{P_0}. \quad (26)$$

Note that the last term ($\delta \tilde{r} \cos \theta / P_0$) corresponds to the “tilt” of the mirror to accomodate the off-axis alignment of the two mirrors (i.e., the fact that $\delta \neq 0$). Furthermore, this tilt term is especially simple when written in cartesian coordinates:

$$\frac{\delta \tilde{r} \cos \theta}{P_0} = \frac{\delta(\tilde{x} - \delta)}{P_0}. \quad (27)$$

It will be useful to have a polar-coordinate version of $h(x, y)$ as well. Put

$$H(r, \theta) = h(x, y). \quad (28)$$

Then from equation (22) and (4)-(5) we find

$$H(r, \theta) = \tilde{H}(\tilde{r}, \theta) - \frac{P_0}{2} - \frac{(\tilde{r} - r)^2 + 2(\tilde{r} - r)\delta \cos(\theta) + \delta^2}{2P_0}. \quad (29)$$

4. Mapping and Apodization Relationship

In this section, we show how to relate the pupil mapping function $R(\tilde{r})$ to a specified amplitude apodization function $A(\tilde{r})$. Here $A(\tilde{r})$ is the geometric gain factor relating the electric field amplitude in the entrance pupil $E(r)$ to that in the exit pupil $\tilde{E}(\tilde{r})$. We assume that A is real. We have

$$\tilde{E}(\tilde{r}) = A(\tilde{r})E(r) \quad (30)$$

where, as above, r and \tilde{r} are related by the specified geometric mapping (equations (6) and (7)).

We now invoke conservation of energy and require that the intensity of light in the entrance pupil $I(r)$ be related to that in the exit pupil $\tilde{I}(\tilde{r})$ by

$$\tilde{I}(\tilde{r})\tilde{r}d\tilde{r}d\theta d\lambda = I(r)rdrd\theta d\lambda \quad (31)$$

where λ is wavelength and intensity is in units of energy per unit time per unit area per wavelength interval.

We then have that $I = |E|^2$ and $\tilde{I} = |\tilde{E}|^2$, in appropriate units. Combining (30) and (31) we get

$$A^2(\tilde{r})\tilde{r}d\tilde{r} = rdr \quad (32)$$

where $r = R(\tilde{r})$. From this it follows that

$$R(\tilde{r})R'(\tilde{r}) = A^2(\tilde{r})\tilde{r}. \quad (33)$$

In other words,

$$(R(\tilde{r})^2)' = 2A^2(\tilde{r})\tilde{r} \quad (34)$$

which can be integrated to yield

$$R(\tilde{r}) = \pm \sqrt{\int_0^{\tilde{r}} 2A^2(s)s ds}. \quad (35)$$

Equation (35) is the fundamental relation that connects the amplitude apodization function A to the ray-mapping function R . In the remainder of this paper, we will develop several results that follow from this relation: In Section 5, we give some explicit examples of pupil mapping. In Section 6, we discuss extensions to different geometries. In Section 7, we discuss replacing the off-axis mirrors with on-axis lenses and derive the corresponding equations for their surfaces. In Section 9, we return to pupil-mapping mirrors and explore the off-axis aberrations analytically.

We end this section by remarking that the relationship between the functions R' and A given for the 1-D case in Traub and Vanderbei (2003) (equation (32)) was derived incorrectly. Fortunately, the correction is simple: just replace A with A^2 in equation (32) and in all subsequent equations that depend on this one.

5. Examples of 2-Mirror Pupil Mapping

5.1. Constant Mapping Function

In this subsection, we choose a constant mapping function and explore its implications. We will find that this simple case leads to a total of 6 different types of 2-mirror systems, depending on the value of the constant. This family includes the familiar afocal Cassegrain, Gregorian, and periscope systems, plus variants on these.

Let us take the intensity mapping function to be

$$A^2(\tilde{r}) = \alpha^2 \quad (36)$$

so that the amplitude mapping function is

$$A(\tilde{r}) = \alpha \quad (37)$$

where we choose the positive root, but allow alpha to take on any real value, positive or negative. From equation (35), the ray-mapping function is then

$$r = R(\tilde{r}) = \alpha\tilde{r}, \quad (38)$$

where again we choose the positive root, with no loss of generality.

Inserting this into equations (26) and (29), and requiring that the first mirror be centered at the origin, $H(0, 0) = 0$, we find the following solutions for the first and second mirror surfaces, respectively:

$$H(r, \theta) = \left(1 - \frac{1}{\alpha}\right) \frac{r^2}{2P_0} - \frac{r\delta \cos \theta}{P_0} \quad (39)$$

$$\tilde{H}(\tilde{r}, \theta) = -(1 - \alpha) \frac{\tilde{r}^2}{2P_0} - \frac{\tilde{r}\delta \cos(\theta)}{P_0} + \frac{P_0}{2} - \frac{\delta^2}{2P_0} \quad (40)$$

For $\alpha \neq 1$, these equations describe paraboloidal mirrors, formed by the rotation of a parabola about an axis parallel to the z axis. For $\alpha = 1$, they describe flat mirrors tilted about axes parallel to the y axis, i.e., a simple periscope.

Setting first derivatives of H and \tilde{H} to zero, we find that the axes of the H and \tilde{H} paraboloids are both centered at

$$(x, y) = \left(\delta \frac{\alpha}{\alpha - 1}, 0\right). \quad (41)$$

The height of the vertex of each paraboloid, either real or projected, is at

$$H_{\min} = -\frac{\delta^2 \alpha}{2P_0(\alpha - 1)} \quad (42)$$

and

$$\tilde{H}_{\max} = \frac{P_0}{2} - \frac{\delta^2 \alpha}{2P_0(\alpha - 1)}. \quad (43)$$

The difference in heights is

$$\tilde{H}_{\max} - H_{\min} = P_0/2 \quad (44)$$

as expected from the property of P_0 as the additional optical path imposed by the two mirrors.

The second derivatives of H and \tilde{H} are the inverse of twice the paraxial focal lengths, i.e., $H_{rr} = 1/(2F)$ and $\tilde{H}_{\tilde{r}\tilde{r}} = -1/(2\tilde{F})$, where the signs are chosen to show that the light is incident on the mirrors from above and below, respectively. Hence, we find these paraxial focal lengths:

$$F = \frac{\alpha P_0}{2(\alpha - 1)} \quad (45)$$

$$\tilde{F} = -\frac{P_0}{2(\alpha - 1)}. \quad (46)$$

The sum of these is $F + \tilde{F} = P_0/2$, indicating that the parabolas have the same focal point (given that their vertices are separated by this amount too), as is expected for a system with parallel light incident on it, and exiting from it.

These properties are summarized in Table 1, and illustrated in Figure 1 which shows an $x - z$ cut through the mirrors and edge rays.

5.2. Gaussian Mapping Function

In the context of searching for extrasolar planets, an ideal coronagraph would concentrate the incident starlight to a very compact image, free of the bright Airy rings that would otherwise be present. The image-plane electric field is the Fourier transform of the pupil-plane electric field, and the Fourier transform of a Gaussian is a Gaussian. Therefore, if we can generate a Gaussian amplitude distribution, the image from such a beam will have small sidelobes, within the approximation that the integral over a finite pupil is approximately the same as the integral over an infinite range. (This latter restriction is removed in Sec. 5.3 where the amplitude will be made equal to a prolate spheroidal function.)

For the Gaussian electric field case, we have the amplitude mapping function

$$A(\tilde{r}) = ce^{-\frac{\tilde{r}^2}{2\sigma^2}} \quad (47)$$

which generates the ray-mapping relation

$$R(\tilde{r}) = \sigma c \sqrt{(1 - e^{-\tilde{r}^2/\sigma^2})}. \quad (48)$$

The constant c is determined by the requirement that $R(\tilde{a}) = a$ and comes out to be

$$c = \frac{a}{\sigma \sqrt{(1 - e^{-\tilde{a}^2/\sigma^2})}}. \quad (49)$$

Hence,

$$R(\tilde{r}) = a \sqrt{\frac{1 - e^{-\tilde{r}^2/\sigma^2}}{1 - e^{-\tilde{a}^2/\sigma^2}}}. \quad (50)$$

The equations for the surfaces H and \tilde{H} can be solved numerically. Typical results are shown in Figures 2 and 3, where both the side view and end view are given, and selected rays are drawn.

5.3. Prolate Spheroidal Wave Functions and Related Apodizations

On a finite interval, the prolate spheroidal wave function plays a role similar to that of a Gaussian on the infinite interval. In particular, for both cases, the product of the width of the function and the width of its Fourier transform is minimal, compared to all other functional forms.

Thus for a coronagraph, a likely optimal design is one in which the electric field across the pupil of an imaging lens is distributed as a prolate spheroidal wave function for 1-D optics and as a generalized prolate spheroidal wave function for 2-D optics (see Slepian (1965)). Kasdin et al. (2004) were the first to notice that these functions play a fundamental role in shaped-pupil coronagraphs. But, it turns out that one can get a slightly tighter inner working angle by using an apodization function that is specifically designed to achieve the desired contrast in the specified dark zone. Optimization models designed in this manner are described in Vanderbei et al. (2003b,c). We show in Figure 4 one such function. In Figure 5 we show the point-spread function illustrating that the sidelobes are lower than 10^{-10} in intensity, nominally adequate for searching for Earth-like planets.

6. Extensions

In this section, we briefly consider some generalizations to the basic set up considered so far.

6.1. Cassegrain vs. Gregorian Design

As we saw in (34), the apodization function A is related to the square of the transfer function R and, in (35), there arose two choices for the square root. Suppose we choose the positive root. Figure 2 shows two views of the resulting optical system associated with the apodization function shown in Figure 4. The first view is of the (x, z) -plane whereas the second view is of the (y, z) -plane. Since the secondary is convex, we refer to this design as a *Cassegrain* design.

If we choose the negative square root, then we arrive at a different optical system—one with a (rather poor) focal plane between the two mirrors. This optical system is shown in Figure 3. We call this design a *Gregorian* design, because the secondary is concave.

The choice between a Cassegrain versus a Gregorian design is largely a question of manufacturability; mathematically they perform the same.

6.2. Concentric (On-Axis) Designs

When the second mirror is assumed to be of smaller aperture than the first, it is possible to consider an on-axis design. In this case, \tilde{R} must map the annulus defined by the interval $[\tilde{a}, a]$ of radii bijectively onto $[0, \tilde{a}]$. All formulas in the previous sections remain unchanged.

7. Refractive Elements

We can replace mirrors \mathcal{M}_1 and \mathcal{M}_2 with coaxial lenses. We require that \mathcal{M}_1 and \mathcal{M}_2 are plano on their outward-facing surfaces, where the entering and exiting rays are parallel (see Figure 6). Assume that the lenses have refractive index n , which is constant over the desired band of wavelengths. It is easy to show that the mirror figures depend only on radius r . Hence, mirror \mathcal{M}_1 's lower surface is defined by a function $h(r)$ and \mathcal{M}_2 's upper surface is given by a function $\tilde{h}(\tilde{r})$. Repeating the derivation at the beginning of section 3 using the refractive form of Snell's law we derive the following analogue of equation (13):

$$h_r(r) = \frac{r - \tilde{r}}{nS + \tilde{h} - h}. \quad (51)$$

And, corresponding to equation (14), we have

$$\tilde{h}_{\tilde{r}}(\tilde{r}) = h_r(r). \quad (52)$$

Interestingly, Lemma 1 changes to:

Lemma 2 $Q_0 = \frac{1}{n}S + \tilde{h} - h$ is a constant.

Hence, the analogue of Theorem 1 is more complicated:

Theorem 2 *The shape of the first lens is determined by the following differential equation:*

$$h_r = \frac{r - \tilde{r}}{\sqrt{n^2 Q_0^2 + (n^2 - 1)(r - \tilde{r})^2}} \quad (53)$$

where \tilde{r} is a known function of r . Similarly, the shape of the second lens is determined by:

$$\tilde{h}_{\tilde{r}} = \frac{r - \tilde{r}}{\sqrt{n^2 Q_0^2 + (n^2 - 1)(r - \tilde{r})^2}}, \quad (54)$$

where r is a known function of \tilde{r} .

Proof. From (51) and Lemma 2, we see that

$$h_r = \frac{r - \tilde{r}}{Q_0 + (n - 1/n)S} \quad (55)$$

Since $S^2 = (r - \tilde{r})^2 + (h - \tilde{h})^2$, we can write the invariant Q_0 as

$$Q_0 = \frac{1}{n}S + \sqrt{S^2 - (r - \tilde{r})^2}. \quad (56)$$

We can rearrange (56) into a quadratic expression in S and then use the formula for the roots of a quadratic equation to express S in terms of Q_0 and $r - \tilde{r}$:

$$S = \frac{-\frac{Q_0}{n} + \sqrt{Q_0^2 + (1 - \frac{1}{n^2})(r - \tilde{r})^2}}{1 - \frac{1}{n^2}}. \quad (57)$$

From this expression, we get that

$$Q_0 + (n - 1/n)S = \sqrt{n^2 Q_0^2 + (n^2 - 1)(r - \tilde{r})^2}. \quad (58)$$

Combining (55) with (58), we get the result claimed. \square

Interestingly, the equivalent of equations (53) and (54) was found by Kreuzer (1969), in a patent application for a pair of lenses that could change the Gaussian-distributed beam from a laser into a sometimes more useful uniform-intensity beam. Since light is reversible, Kreuzer’s goal and ours are essentially the same. Both before and after Kreuzer’s discovery, there have been many papers pursuing similar ends; as a recent example, we mention Hoffnagle and Jefferson (2003), who designed and fabricated a pair of convex lenses for this purpose. Our example, shown in Figure 6, was derived using equations (47)–(50), with a value $c > 0$, and gives one positive and one negative lens. If we had used $c < 0$, we would have found both lenses to be positive, and this is effectively what Hoffnagle and Jefferson did in their experiment.

8. Mapping Elliptical Pupils to Circular Ones

The current baseline design for the Terrestrial Planet Finder space telescope involves an $8 \times 3.5\text{m}$ primary mirror and a square downstream deformable mirror for wavefront control. This disparity of shapes introduces the need to reshape the pupil using anamorphic mirrors, which

introduces the opportunity also to develop unique pairs of anamorphic mirrors so as to apodize the exit pupil as desired for high-contrast imaging. We discuss this design problem here. So, we assume that mirror \mathcal{M}_1 is elliptical having semimajor axes a and b : $\{(x, y) : (x/a)^2 + (y/b)^2 \leq 1\}$. We assume that \mathcal{M}_2 is a circular mirror of radius \tilde{a} , that \mathcal{M}_1 is uniformly illuminated, and that the beam leaving mirror \mathcal{M}_2 is apodized according to a given function $A(\tilde{r})$ that depends only on the radius \tilde{r} . In this setup, the obvious hope would be that the transfer function \tilde{R} from the circular case can simply be stretched as needed at each angle θ :

$$\tilde{r} = \tilde{R} \left(\frac{r\tilde{a}}{ab} \sqrt{a^2 \sin^2 \theta + b^2 \cos^2 \theta} \right) \quad (59)$$

(the scaling of r inside the function \tilde{R} is chosen so that the result will be between 0 and \tilde{a}). But, this transformation implies that the simple angular map $\tilde{\theta} = \theta$ is no longer adequate; we need to introduce a θ -transfer function

$$\theta = \Theta(\tilde{\theta}) \quad (60)$$

and its inverse

$$\tilde{\theta} = \tilde{\Theta}(\theta). \quad (61)$$

Given this, the inverse transformation for \tilde{R} is easy to find:

$$r = \frac{ab/\tilde{a}}{\sqrt{a^2 \sin^2 \Theta(\tilde{\theta}) + b^2 \cos^2 \Theta(\tilde{\theta})}} R(\tilde{r}). \quad (62)$$

From the usual change of variables, we get that

$$r dr d\theta = \frac{a^2 b^2 / \tilde{a}^2}{a^2 \sin^2 \Theta(\tilde{\theta}) + b^2 \cos^2 \Theta(\tilde{\theta})} R(\tilde{r}) R'(\tilde{r}) \Theta'(\tilde{\theta}) d\tilde{r} d\tilde{\theta} \quad (63)$$

and our aim is to have

$$r dr d\theta = A(\tilde{r})^2 \tilde{r} d\tilde{r} d\tilde{\theta}. \quad (64)$$

Combining (63) and (64), we see that

$$A(\tilde{r})^2 \tilde{r} = R(\tilde{r}) R'(\tilde{r}) \frac{\gamma}{\tilde{a}^2} \quad (65)$$

$$\frac{a^2 b^2}{a^2 \sin^2 \Theta(\tilde{\theta}) + b^2 \cos^2 \Theta(\tilde{\theta})} \Theta'(\tilde{\theta}) = \gamma. \quad (66)$$

where γ is a constant determined by a boundary condition to be discussed shortly. Integrating differential equation (66), we get that

$$\tilde{\theta} = \frac{ab}{\gamma} \tan^{-1} \left(\frac{a}{b} \tan \theta \right). \quad (67)$$

Since $\theta = \pi/2$ when $\tilde{\theta} = \pi/2$, it follows that

$$\gamma = ab. \quad (68)$$

Hence,

$$\tilde{\Theta}(\theta) = \tan^{-1} \left(\frac{a}{b} \tan \theta \right), \quad (69)$$

$$\Theta(\tilde{\theta}) = \tan^{-1} \left(\frac{b}{a} \tan \tilde{\theta} \right), \quad (70)$$

and $R(\tilde{r})$ is determined by integrating

$$A(\tilde{r})^2 \tilde{r} = R(\tilde{r}) R'(\tilde{r}) \frac{ab}{\tilde{a}^2}. \quad (71)$$

Converting polar functions $R(\tilde{r})$ and $\Theta(\tilde{\theta})$ into cartesian equations for x and y as functions of \tilde{x} and \tilde{y} , we can finally calculate the mirror shapes using the differential equations in Theorem 1.

9. Off-Axis Performance

In this section we do a careful ray-trace analysis for an off-axis source. Suppose that the infinitely remote source lies in the (x, z) -plane and is oriented at an angle ϕ from vertical so that its unit incidence vector is $(-\sin \phi, 0, \cos \phi)$. To keep the analysis manageable, we will only trace rays in the (x, z) -plane. In polar coordinates, this is the (r, z) -plane and $\theta = 0$. The incoming rays can be parametrized by the x -coordinate at which they hit the first mirror. Fix an x and consider such a ray. A ray trace is shown in Figure 7. Throughout this section, anytime a function is a function of y or \tilde{y} (among other variables), we will suppress this dependence since these variables are zero in this section. Also, for notational convenience we extend the definitions of functions R and \tilde{R} to negative values by making the functions odd:

$$R(-\tilde{r}) = -R(\tilde{r}) \quad \text{and} \quad \tilde{R}(-r) = -\tilde{R}(r). \quad (72)$$

Since the rays are entering the system at an angle, the place where the reflection hits the second mirror is displaced, say by $\Delta\tilde{x}$, from the point \tilde{x} where an on-axis ray hit this second mirror. We begin with this displacement.

Lemma 3 $\Delta\tilde{x} = S(x, \tilde{x})\phi + o(\phi)$.

Proof. This is exactly Lemma 1 in Traub and Vanderbei (2003). □

A second quantity of importance is the angle $\tilde{\phi}$ at which a light ray reflects off from the second mirror. We are interested in how this angle depends on the position x and angle ϕ at which it hit the first mirror:

Lemma 4 $\tilde{\phi} = \frac{\phi}{\tilde{R}'(x)} + o(\phi)$.

Proof. This is essentially Lemma 2 from Traub and Vanderbei (2003). More specifically, it follows directly from equations (15) and (16) in the proof of Lemma 2 in Traub and Vanderbei (2003) that

$$\tilde{\phi} \approx \frac{dx/d\tilde{x}}{S(x, \tilde{x})} \Delta\tilde{x} = \frac{dx}{d\tilde{x}} \phi. \quad (73)$$

Then, $dx/d\tilde{x}(\tilde{x}) = R'(\tilde{x}) = 1/\tilde{R}'(x)$. □

Lemmas 3 and 4 tell us that a ray incident on the first mirror at x -coordinate x and angle ϕ bounces off the second mirror at x -coordinate $\tilde{x}(x) + S\phi = \tilde{R}(x) + \delta + S\phi$ and at angle $\phi/\tilde{R}'(x)$. We summarize this by writing

$$\{x, \phi\} \xrightarrow{\mathcal{M}_1 \rightarrow \mathcal{M}_2} \left\{ \tilde{R}(x) + \delta + S(x, \tilde{x})\phi, \quad \frac{\phi}{\tilde{R}'(x)} \right\}. \quad (74)$$

Lemma 4 is both good and bad. It is good because, for apodizations of interest, $\tilde{R}'(x)$ is less than one for most x 's and hence there is a built-in magnification—off-axis rays come out of the system at a steeper angle than they had on entry. It is bad because the rays are no longer parallel and therefore cannot be focused to a diffraction-limited image.

We discuss in detail the issue of nonparallel rays, and how to remedy it, in the next section. We end this section with some further discussion of the magnification effect. It turns out to be most convenient to consider $\tilde{\phi}$ parametrized over \tilde{r} rather than over r . That is, we are interested in

$$\tilde{\phi}(\tilde{r}) \approx \frac{\phi}{\tilde{R}'(\tilde{R}(\tilde{r}))} \quad (75)$$

$$= R'(\tilde{r})\phi \quad (76)$$

$$= \frac{A(\tilde{r})^2 \tilde{r} \phi}{\sqrt{\int_0^{\tilde{r}} 2A(s)^2 s ds}}. \quad (77)$$

Here, the last equality follows from (35). To arrive at an average magnification, we take an intensity-weighted average of $\tilde{\phi}(\tilde{r})/\phi$:

$$\text{magnif} = \frac{\int_0^{\tilde{a}} \tilde{\phi}(\tilde{r}) A(\tilde{r})^2 \tilde{r} d\tilde{r}}{\phi \int_0^{\tilde{a}} A(\tilde{r})^2 \tilde{r} d\tilde{r}}. \quad (78)$$

9.1. Pupil Restoration by System Reversal

Guyon (2003) addresses this off-axis defocus question. He recommends placing a focusing element \mathcal{L}_1 after \mathcal{M}_2 followed by a star occulter in the image plane, a beam-recollimating element \mathcal{L}_2 , and finally a pupil mapping system identical to the first two mirrors but set up exactly backwards. Let's refer to these last two mirrors as \mathcal{M}_3 and \mathcal{M}_4 . If the focusing and recollimating elements (\mathcal{L}_1 and \mathcal{L}_2) are assumed to be ideal lenses having a common focal length, say f , and if the distances from \mathcal{M}_2 to \mathcal{L}_1 and from \mathcal{L}_2 to \mathcal{M}_3 are both also chosen to be f , then the pupil at mirror \mathcal{M}_3 is a reimaging of the pupil at \mathcal{M}_2 and so a ray hitting \mathcal{M}_2 at, say, position \tilde{x} and angle $\tilde{\phi}$ will hit \mathcal{M}_3 at position $2\delta - \tilde{x}$ and angle $-\tilde{\phi}$. We summarize this as

$$\left\{ \tilde{x}, \tilde{\phi} \right\} \xrightarrow{\mathcal{M}_2 \rightarrow \mathcal{M}_3} \left\{ 2\delta - \tilde{x}, -\tilde{\phi} \right\} \quad (79)$$

(see Figure 8).

Figure 9 shows a version of the full system in which the reversed system folds back to the left. The following theorem describes how an off-axis ray propagates from mirror \mathcal{M}_3 to \mathcal{M}_4 .

Theorem 3 *For the system shown in Figure 9, a ray propagates from mirror \mathcal{M}_3 to mirror \mathcal{M}_4 as follows:*

$$\left\{ \tilde{x}, \tilde{\phi} \right\} \xrightarrow{\mathcal{M}_3 \rightarrow \mathcal{M}_4} \left\{ R(\tilde{x} - \delta) + S(\hat{x}, \tilde{x})\tilde{\phi}, \frac{\tilde{\phi}}{R'(\tilde{x} - \delta)} \right\} \quad (80)$$

where \hat{x} denotes the point on mirror \mathcal{M}_4 corresponding to an on-axis ray impinging on mirror \mathcal{M}_3 at \tilde{x} .

Proof. Because the reversed pupil mapping system ($\mathcal{M}_3, \mathcal{M}_4$) is identical to the first one, we start by inverting the operation given by (74). This inversion describes a ray propagating backwards through mirrors \mathcal{M}_2 and \mathcal{M}_1 .

From (74), we have that

$$\tilde{\phi} = \frac{\phi}{\tilde{R}'(x)}. \quad (81)$$

Hence,

$$\phi = \tilde{R}'(x)\tilde{\phi}. \quad (82)$$

We need to express $\tilde{R}'(x)$ in terms of \tilde{x} (and perhaps $\tilde{\phi}$). To this end, we use equations (5), (6), and (7) to write

$$\tilde{x} = \tilde{r} + \delta = \tilde{R}(r) + \delta = \tilde{R}(R(\tilde{r})) + \delta = \tilde{R}(R(\tilde{x} - \delta)) + \delta. \quad (83)$$

Differentiating with respect to \tilde{x} , we get

$$1 = \tilde{R}'(R(\tilde{x} - \delta))R'(\tilde{x} - \delta). \quad (84)$$

Hence,

$$\tilde{R}'(x)R'(\tilde{x} - \delta) = 1 \quad (85)$$

and so we get that

$$\phi = \frac{\tilde{\phi}}{R'(\tilde{x} - \delta)}. \quad (86)$$

Now, we remind the reader that our propagations represent just the constant and linear terms in an expansion in the small angular parameters ϕ and $\tilde{\phi}$. Since these angles are small, it follows that $\tilde{x} - \tilde{x}$ is also small. We retain terms that are linear in these small parameters but we drop higher order terms. Hence, since the right-hand side in (86) already is small, we can simply replace $R'(\tilde{x} - \delta)$ with $R'(\tilde{x} - \delta)$.

From (74), we also have that

$$\tilde{x} = \tilde{R}(x) + \delta + S(x, \tilde{x})\phi. \quad (87)$$

We need to solve this for x . From (8), we see that

$$x = R(\tilde{x} - \delta - S(x, \tilde{x})\phi) \quad (88)$$

$$\approx R(\tilde{x} - \delta) - R'(\tilde{x} - \delta)S(x, \tilde{x})\phi \quad (89)$$

$$= R(\tilde{x} - \delta) - S(x, \tilde{x})\tilde{\phi} \quad (90)$$

$$\approx R(\tilde{x} - \delta) - S(\hat{x}, \tilde{x})\tilde{\phi}, \quad (91)$$

where \hat{x} denotes the point on mirror \mathcal{M}_1 corresponding to an on-axis ray impinging on mirror \mathcal{M}_2 at \tilde{x} .

From (86) and (91), we see that backwards propagation through the \mathcal{M}_1 - \mathcal{M}_2 system is given by

$$\left\{ \tilde{x}, \tilde{\phi} \right\} \xrightarrow{\mathcal{M}_2 \rightarrow \mathcal{M}_1} \left\{ R(\tilde{x} - \delta) - S(\hat{x}, \tilde{x})\tilde{\phi}, \quad \frac{\tilde{\phi}}{R'(\tilde{x} - \delta)} \right\}. \quad (92)$$

To describe propagation through the \mathcal{M}_3 - \mathcal{M}_4 system, we have to flip this system about a horizontal axis, apply the above transformation, and then flip back. The flip operation leaves horizontal coordinates unchanged but negates angles. Hence, we get

$$\{\tilde{x}, \tilde{\phi}\} \longrightarrow \{\tilde{x}, -\tilde{\phi}\} \quad (93)$$

$$\longrightarrow \left\{ R(\tilde{x} - \delta) + S(\hat{x}, \tilde{x})\tilde{\phi}, \quad -\frac{\tilde{\phi}}{R'(\tilde{x} - \delta)} \right\} \quad (94)$$

$$\longrightarrow \left\{ R(\tilde{x} - \delta) + S(\hat{x}, \tilde{x})\tilde{\phi}, \quad \frac{\tilde{\phi}}{R'(\tilde{x} - \delta)} \right\}. \quad (95)$$

This completes the proof. \square

We are now ready to combine the above ray propagation results to describe propagation through the entire system:

Theorem 4 *For the system shown in Figure 9, a ray entering the system at position x and angle ϕ , exits the system at position $-x - 2\frac{S(x, \tilde{x})}{\tilde{R}'(x)}\phi$ and at angle $\frac{-\phi}{1 - \frac{\tilde{R}''(x)}{\tilde{R}'(x)^2}S(x, \tilde{x})\phi}$.*

Proof. We can compose the maps given by (74), (79), and (80) to get that

$$\{x, \phi\} \longrightarrow \left\{ \tilde{R}(x) + \delta + S(x, \tilde{x})\phi, \quad \frac{\phi}{\tilde{R}'(x)} \right\} \quad (96)$$

$$\longrightarrow \left\{ -\tilde{R}(x) + \delta - S(x, \tilde{x})\phi, \quad -\frac{\phi}{\tilde{R}'(x)} \right\} \quad (97)$$

$$\longrightarrow \left\{ R\left(-\tilde{R}(x) - S(x, \tilde{x})\phi\right) - \frac{S(x, \tilde{x})\phi}{\tilde{R}'(x)}, \quad -\frac{\phi}{\tilde{R}'(x)R'\left(-\tilde{R}(x) - S(x, \tilde{x})\phi\right)} \right\} \quad (98)$$

Since $R(\tilde{R}(x)) = x$, we can differentiate this identity to derive simple identities relating the derivatives of $R(\tilde{R}(x))$ to the derivatives of $\tilde{R}(x)$. From these identities, we easily see that

$$R\left(\tilde{R}(x) + S(x, \tilde{x})\phi\right) = R(\tilde{R}(x)) + R'(\tilde{R}(x))S(x, \tilde{x})\phi + o(\phi) \quad (99)$$

$$= x + \frac{S(x, \tilde{x})}{\tilde{R}'(x)}\phi + o(\phi) \quad (100)$$

and

$$R' \left(\tilde{R}(x) + S(x, \tilde{x})\phi \right) = R'(\tilde{R}(x)) + R''(\tilde{R}(x))S(x, \tilde{x})\phi + o(\phi) \quad (101)$$

$$= \frac{1}{\tilde{R}'(x)} - \frac{\tilde{R}''(x)}{\tilde{R}'(x)^3} S(x, \tilde{x})\phi + o(\phi) \quad (102)$$

Using the fact that R is an odd function, and therefore that R' is even, we substitute (100) and (102) into (98) to get the results claimed in the theorem. \square

A comparison of the exiting ray angles from the 4-mirror corrected system (Theorem 4) compared to those from the 2-mirror uncorrected system (Lemma 2) shows that the relative scatter of ray angles will be smaller in the corrected system by a factor which depends on the details of the function \tilde{R} , but which in general will be roughly a factor of a few times the off-axis angle ϕ ; for typical planet-searching angles of a few arcseconds, this ratio could easily be less than 10^{-3} , which is a significant reduction in scatter of ray angles. (Specific estimates will be given in a future paper with numerical results.)

Figure 10 shows a version of the full system in which the reversed pupil mapping folds off to the right. This case is just like the previous one except that there is effectively a symmetry reflection about the vertical axis $x = \delta$ that must be applied before entering and after leaving the second system. Flipping about this vertical axis has the effect given by (79).

Theorem 5 *For the system shown in Figure 10, a ray entering the system at position x and angle ϕ , exits the system at position $2\delta - x - 2\frac{S(x, \tilde{x})}{\tilde{R}'(x)}\phi$ and at angle $\frac{-\phi}{1 - \frac{\tilde{R}''(x)}{\tilde{R}'(x)^2}S(x, \tilde{x})\phi}$.*

Proof. We need to compose the maps given by (74), (79), (79), (80), and (79). Of course, applying (79) twice in a row simply undoes the effect and so we can simply form the composition of (74),

(80), and (79):

$$\{x, \phi\} \longrightarrow \left\{ \tilde{R}(x) + \delta + S(x, \tilde{x})\phi, \quad \frac{\phi}{\tilde{R}'(x)} \right\} \quad (103)$$

$$\longrightarrow \left\{ R \left(\tilde{R}(x) + S(x, \tilde{x})\phi \right) + \frac{S(x, \tilde{x})\phi}{\tilde{R}'(x)}, \quad \frac{\phi}{\tilde{R}'(x)R' \left(\tilde{R}(x) + S(x, \tilde{x})\phi \right)} \right\} \quad (104)$$

$$= \left\{ x + 2\frac{S(x, \tilde{x})}{\tilde{R}'(x)}\phi, \quad \frac{\phi}{1 - \frac{\tilde{R}''(x)}{\tilde{R}'(x)^2}S(x, \tilde{x})\phi} \right\} \quad (105)$$

$$\longrightarrow \left\{ 2\delta - x - 2\frac{S(x, \tilde{x})}{\tilde{R}'(x)}\phi, \quad -\frac{\phi}{1 - \frac{\tilde{R}''(x)}{\tilde{R}'(x)^2}S(x, \tilde{x})\phi} \right\}. \quad (106)$$

□

Since the estimated aberrations x and ϕ are the same in Theorems 4 and 5 (cf. Figures 9 and 10), we see that these correcting schemes are equivalent in terms of their ability to reduce aberrations.

Finally, we remark that our analysis has ignored the beam walk that would be introduced by the fact that mirrors \mathcal{M}_2 and \mathcal{M}_3 are not everywhere a distance f from the corresponding lens.

10. Summary

We derived equations for the shapes of mirrors and lenses capable of converting a uniform-intensity beam into a shaped-intensity beam (the pupil-mapping process). We gave analytical estimates of the aberrations of a 2-mirror system, and the improved case of an aberration-corrected 4-mirror system. We applied the results to several examples, including the familiar Cassegrain-Gregorian telescope designs, as well as beam shapes given by Gaussian and prolate spheroidal functions. The general equations will allow the design of many types of optical systems, but in particular should be helpful in designing optics for telescopic searches for extrasolar planets.

Acknowledgements. This research was partially performed for the Jet Propulsion Laboratory, California Institute of Technology, sponsored by the National Aeronautics and Space Administration as part of the TPF architecture studies and also under JPL subcontract number 1260535. The first author received support from the NSF (CCR-0098040) and the ONR (N00014-98-1-0036).

REFERENCES

- C. Aime and R. Soummer, editors. *Astronomy with High Contrast Imaging*, volume 8. ESA Publications Series, 2003.
- D.J. DesMarais, M. Harwit, K. Jucks, J. Kasting, D. Lin, J. Lunine, J. Schneider, S. Seager, W. Traub, and N. Woolf. Remote sensing of planetary properties and biosignatures on extrasolar terrestrial planets. *Astrobiology*, 2002.
- R. Galicher, O. Guyon, S. Ridgway, H. Suto, and M. Otsubo. Laboratory demonstration and numerical simulations of the phase-induced amplitude apodization. In *Proceedings of the 2nd TPF Darwin Conference*, 2004.
- A. Goncharov, M. Owner-Petersen, and D. Puryayev. Intrinsic apodization effect in a compact two-mirror system with a spherical primary mirror. *Opt. Eng.*, 41(12):3111, 2002.
- O. Guyon. Phase-induced amplitude apodization of telescope pupils for extrasolar terrestrial planet imaging. *Astronomy and Astrophysics*, 404:379–387, 2003.
- J.A. Hoffnagle and C.M. Jefferson. Beam shaping with a plano-aspheric lens pair. *Opt. Eng.*, 42(11):3090–3099, 2003.
- N. J. Kasdin, R. J. Vanderbei, M. G. Littman, and D. N. Spergel. Optimal one-dimensional apodizations and shaped pupils for planet finding coronagraphy. *Applied Optics*, 2004. To appear.
- J.L. Kreuzer. Coherent light optical system yielding an output beam of desired intensity distribution at a desired equiphase surface, Nov 1969. U.S. Patent Number 3,476,463.
- M. J. Kuchner and W. A. Traub. A coronagraph with a band-limited mask for finding terrestrial planets. *The Astrophysical Journal*, (570):900, 2002.
- M.J. Kuchner, J. Crepp, and J. Ge. Finding terrestrial planets using eighth-order image masks. *Submitted to The Astrophysical Journal*, 2004. (astro-ph/0411077).
- M.J. Kuchner and D.N. Spergel. Terrestrial planet finding with a visible light coronagraph. In D. Deming and S. Seager, editors, *Scientific Frontiers in Research on Extrasolar Planets*, ASP Conf. Ser. 294, pages 603–610, 2003.
- B.M. Levine, M. Shao, D.T. Liu, J.K. Wallace, and B.F. Lane. Planet detection in visible light with a single aperture telescope and nulling coronagraph. In *Proceedings of SPIE Conference on Astronomical Telescopes and Instrumentation*, 5170, pages 200–208, 2003.

- P. Nisenson and C. Papaliolios. Detection of earth-like planets using apodized telescopes. *The Astrophysical Journal*, 548(2):L201–L205, 2001.
- D. Slepian. Analytic solution of two apodization problems. *Journal of the Optical Society of America*, 55(9):1110–1115, 1965.
- D. N. Spergel. A new pupil for detecting extrasolar planets. *astro-ph/0101142*, 2000.
- W.A. Traub and R.J. Vanderbei. Two-Mirror Apodization for High-Contrast Imaging. *Astrophysical Journal*, 599:695–701, 2003.
- R. J. Vanderbei, N. J. Kasdin, and D. N. Spergel. Rectangular-mask coronagraphs for high-contrast imaging. *Astrophysical Journal*, 2004. To appear.
- R.J. Vanderbei, N.J. Kasdin, and D.N. Spergel. New pupil masks for high-contrast imaging. In *Proceedings of SPIE Conference on Astronomical Telescopes and Instrumentation*, number 07 in 5170, 2003a.
- R.J. Vanderbei, D.N. Spergel, and N.J. Kasdin. Circularly Symmetric Apodization via Starshaped Masks. *Astrophysical Journal*, 599:686–694, 2003b.
- R.J. Vanderbei, D.N. Spergel, and N.J. Kasdin. Spiderweb Masks for High Contrast Imaging. *Astrophysical Journal*, 590:593–603, 2003c.

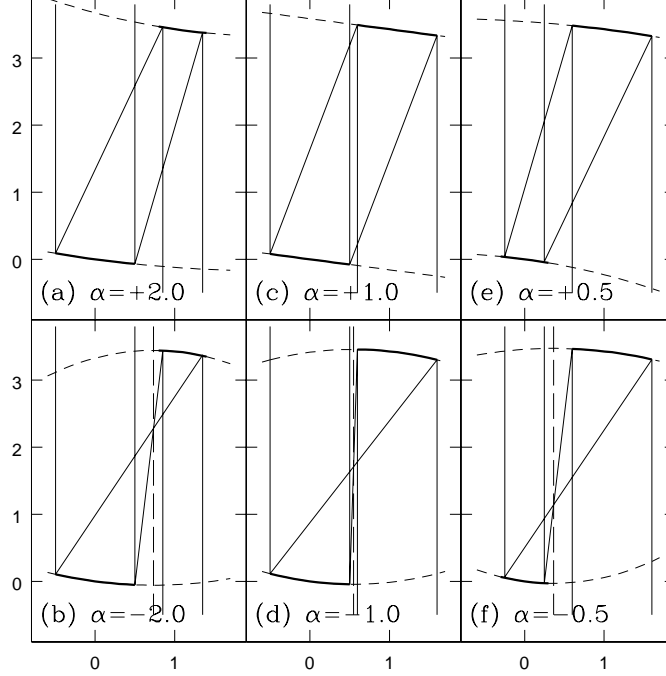


Fig. 1.— This figure shows the family of 6 types of 2-mirror systems that can be obtained from the requirement that an input beam with a flat wavefront be mapped to an output beam also with a flat wavefront but with a uniform relative intensity of α^2 . The short dashed lines show the large-scale surface of revolution of each paraboloid. The heavy solid line shows the actual mirror surface. The long dashed line shows the common axis of revolution of the surfaces (outside the panel in the upper 3 panels). In each case the vertices have the same vertical separation ($P_0/2 = 3.5$) and horizontal separation ($\delta = 1.1$), and the diameter of the larger mirror is 1. Input is from the upper left, and output is to the lower right. (a) Cassegrain with $\alpha > 1$; confocal paraboloids, with common focus outside the panel (above and right). (b) Gregorian with $\alpha < -1$; confocal paraboloids with common focus between the mirrors and on the axis of each mirror, as shown. (c) Symmetric Cassegrain (periscope), $\alpha = 1$; two flat mirrors, common axis and focus at infinity. (d) Symmetric Gregorian, $\alpha = -1$; confocal paraboloids, with focal points geometrically centered as shown. (e) Inverted Cassegrain, $0 < \alpha < 1$; confocal paraboloids with common focus outside panel, exactly the same as (a) for reversed direction of light beam and $\alpha \rightarrow 1/\alpha$. (f) Inverted Gregorian, $-1 < \alpha < 0$; confocal paraboloids with focus between the mirrors, same as (b) for reversed light and inverse α .

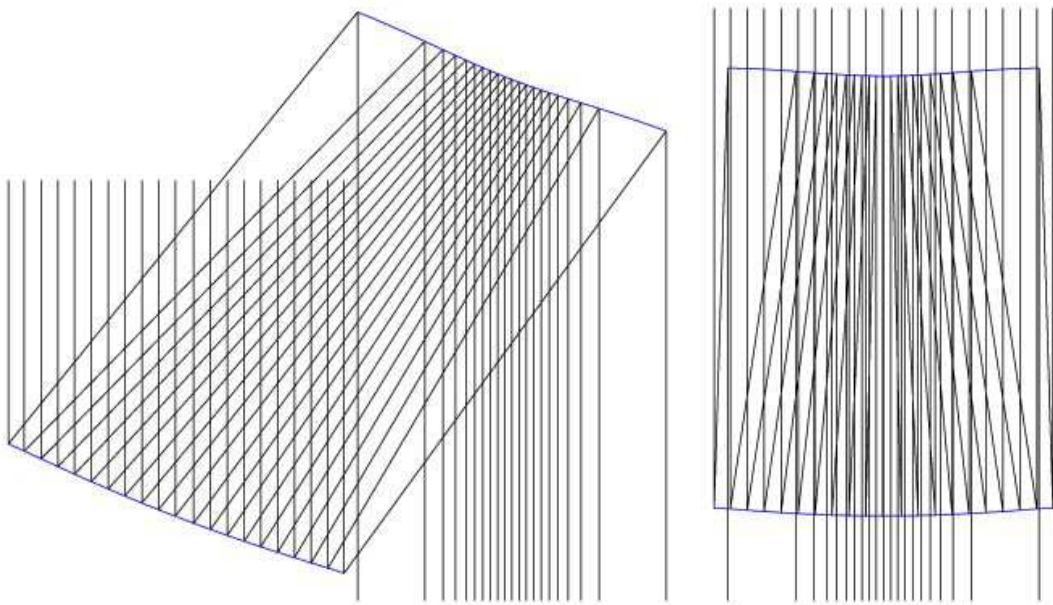


Fig. 2.— A Cassegrain design. Parallel light rays come down from above, reflect off the bottom mirror, bounce up to the top mirror, and then exit downward as a parallel bundle with a concentration of rays in the center of the bundle and thinning out toward the edges—that is, the exit bundle is apodized, but with no loss of light.

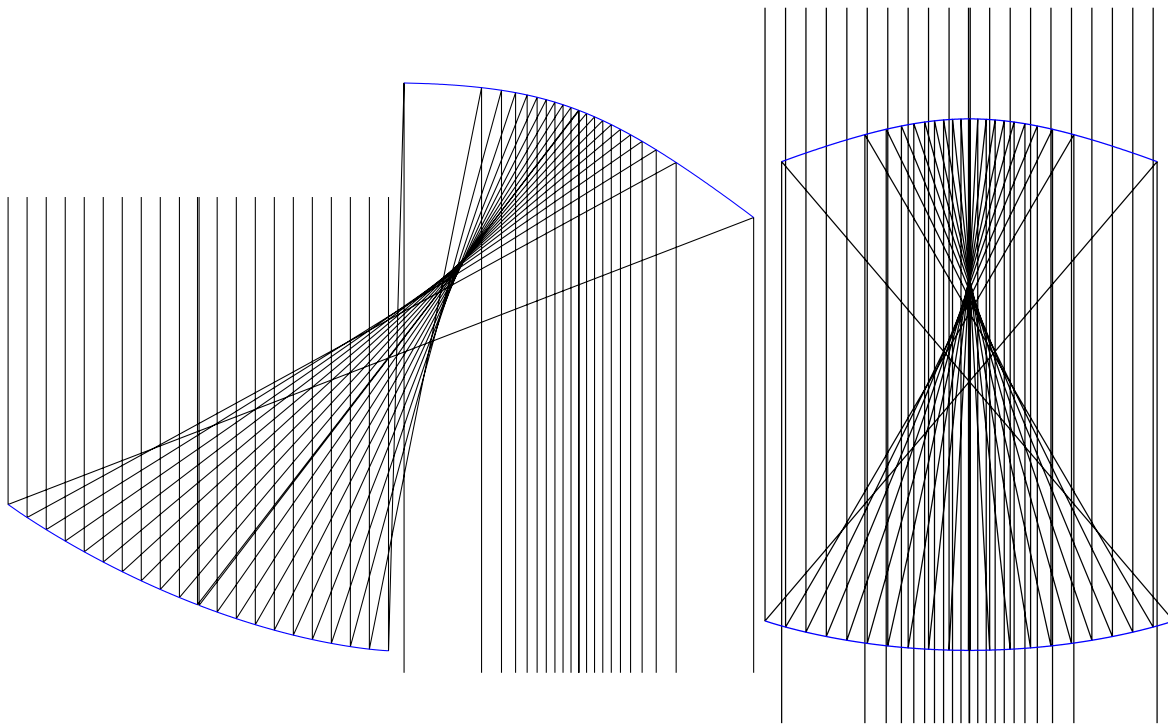


Fig. 3.— A Gregorian design. Similar to Figure 2, but since both mirrors are concave there is an intermediate focus, albeit a poor focus with a large halo. Nevertheless the rays emerge parallel, just as in Figure 2. An advantage here might be in manufacturability.

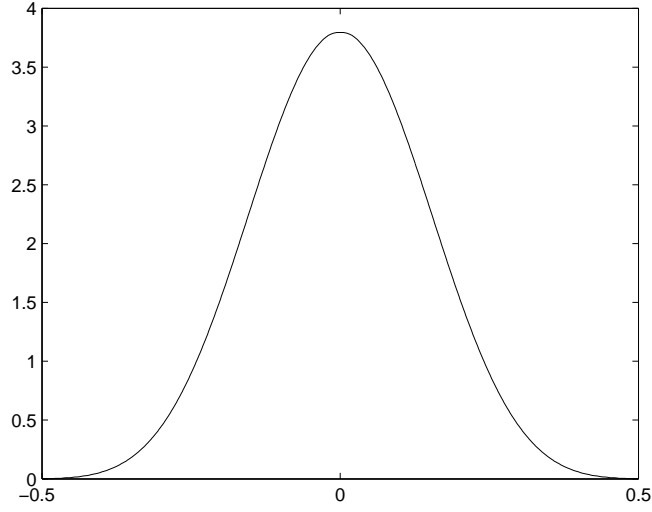


Fig. 4.— An energy conserving apodization providing contrast of 10^{-10} from $4\lambda/D$ to $60\lambda/D$. As explained in Section 9 (and in Traub and Vanderbei (2003)), the unitless angle $4\lambda/D$ only corresponds to a sky angle in the case where the apodization function is identically one. For non-trivial apodizations, such as this one, the off-axis rays get magnified by a factor related to $A(r)$. Hence, the intensity-weighted average magnification given by (78) (using (77)) evaluates to 2.16 and therefore $4\lambda/D$ corresponds to $(4/2.16)\lambda/D = 1.85\lambda/D$ as an angle on the sky.

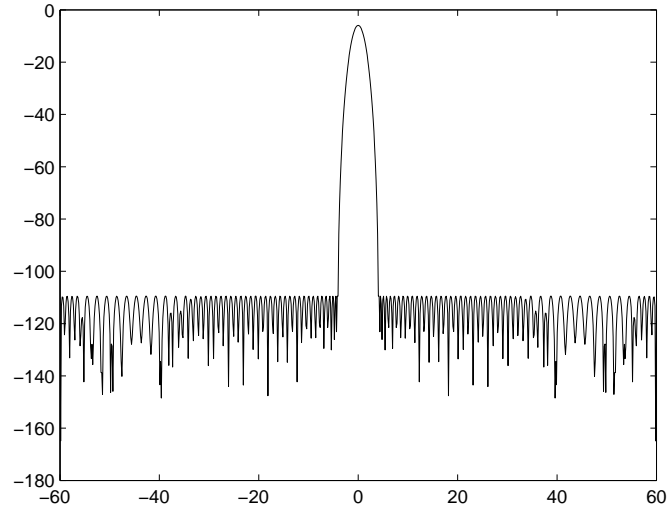


Fig. 5.— The on-axis point spread function for the apodization shown in Figure 4. High contrast for an on-axis point source occurs at $4\lambda/D$. But, as explained in the previous caption, an off-axis source such as a planet having, say, an angle of $2\lambda/D$ in the sky will appear mostly at 2×2.16 or $4.32\lambda/D$ and is therefore detectable in principle.

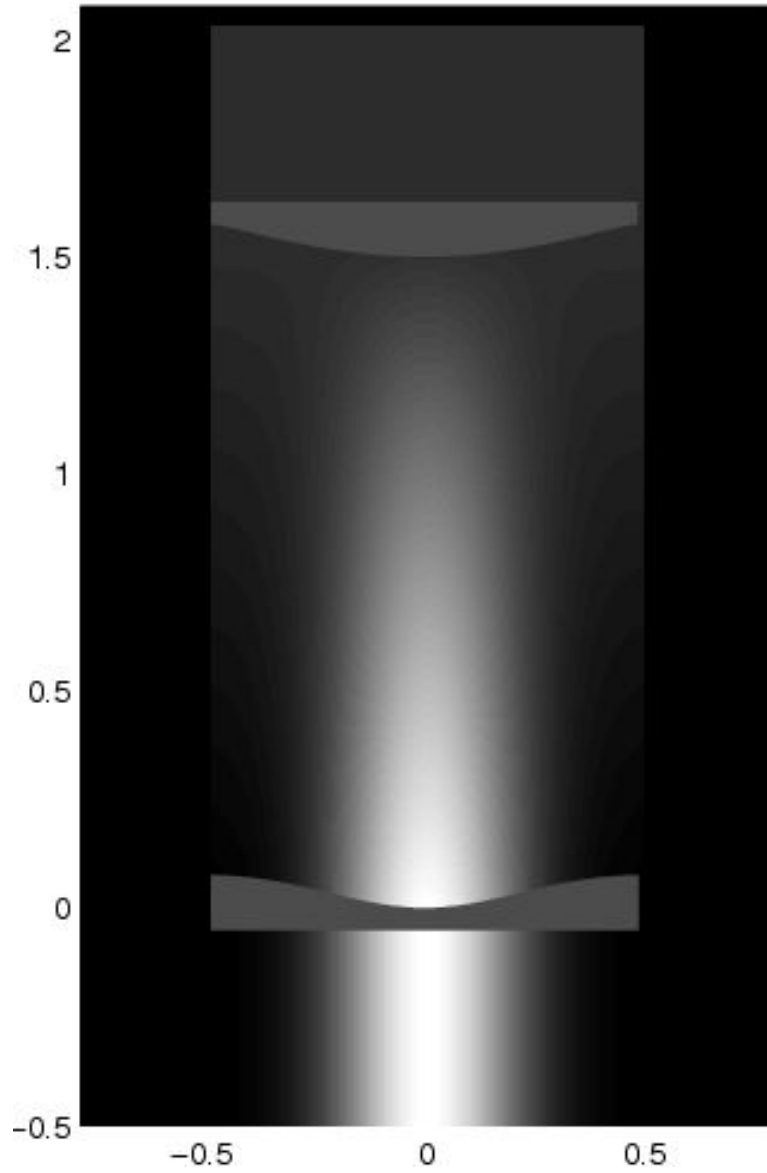


Fig. 6.— Pupil mapping via a pair of properly figured lenses. This Galilean arrangement, with one convex and one concave lens, is the result of using $c > 0$ in the Gaussian mapping function in Eqns. (47)–(49). If we had used $c < 0$ the resulting lenses would both be convex, and the beam would have had a waist (an approximate focus) between the lenses.

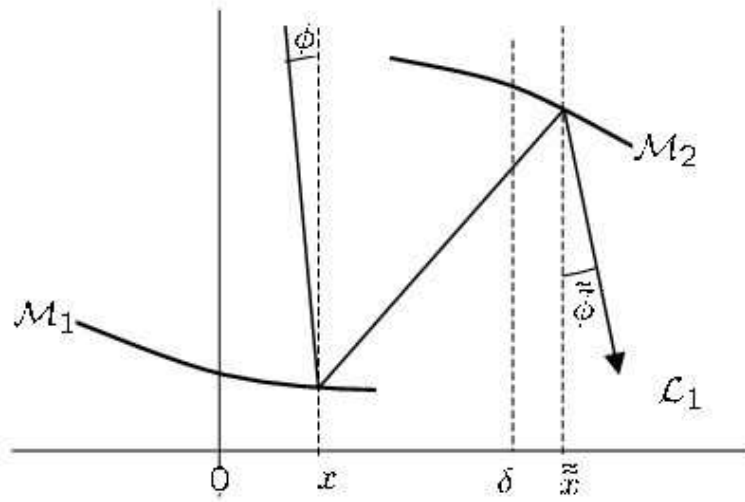


Fig. 7.— Ray-trace of an off-axis source as it passes through a two-mirror pupil mapper.

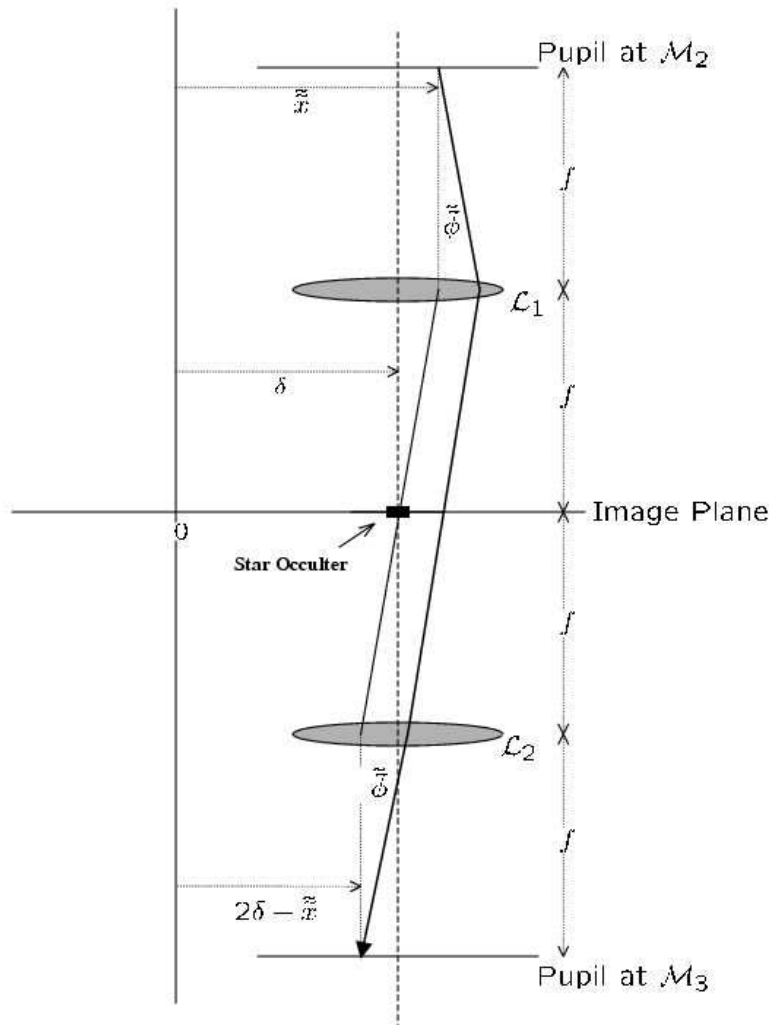


Fig. 8.— Ray-trace of an off-axis source from \mathcal{M}_2 to \mathcal{M}_3 for a 4-mirror system. Note that by placing the lenses halfway between their corresponding mirrors and the image plane and choosing their focal lengths to be this distance, we get that the image of mirror \mathcal{M}_2 is exactly at \mathcal{M}_3 . Hence, each ray maps to a position reflected through the optical axis and comes out with the opposite direction.

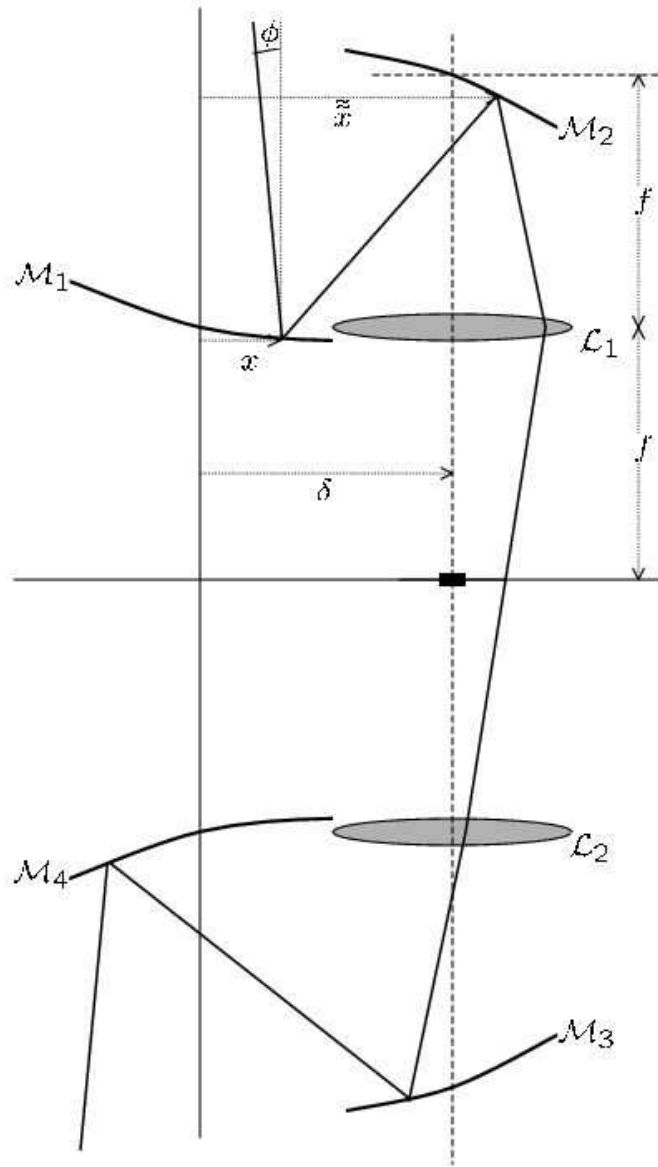


Fig. 9.— Ray-trace for the full 4-mirror system: two-mirror pupil mapper, lens system, and reversed two-mirror pupil mapper. An occulting spot is shown at the center of the image plane to block on-axis starlight.

Quantity (units)	$\alpha < -1$	$\alpha = -1$	$-1 < \alpha < 0$	$0 < \alpha < 1$	$\alpha = 1$	$\alpha > 1$
$x_{\min} = \tilde{x}_{\max} (\delta)$	1 to $1/2$	$1/2$	$1/2$ to 0	0 to $-\infty$	$\pm\infty$	∞ to 1
$H_{\min} (\frac{\delta^2}{2P_0})$	-1 to $-1/2$	$-1/2$	$-1/2$ to 0	0 to ∞	$\pm\infty$	$-\infty$ to -1
sign of F	+	+	+	-	∞	+
sign of \tilde{F}	+	+	+	+	∞	-
type of system	Greg.	eq. Greg.	inv. Greg.	Cass.	eq. Cass.	inv. Cass.

Table 1: Characteristics of 2-mirror afocal systems, generated from the amplitude mapping function $A(\tilde{r}) \equiv \alpha$. Here, *inv.* means inverted, *eq.* means equal and refers to relative mirror sizes, *Greg.* means Gregorian, and *Cass.* means Cassegrain. Note that the “equal Cass.” is a plane-mirror periscope.